This is the Pre-Published Version.

IEEE TRANSACTIONS ON INDUSTRIAL ELECTRONICS

The following publication Z. Li, S. Niu, M. Jiang, Z. Lyu, W. Liu and K. T. Chau, "An Integrated Toroidal Winding Design for Open-Winding Magnetless Vernier Reluctance Linear Machine in Long-Stroke Module," in IEEE Transactions on Industrial Electronics, vol. 73, no. 2, pp. 2779-2790, Feb. 2026 is available at https://doi.org/10.1109/TIE.2025.3595982.

An Integrated Toroidal Winding Design for Open-Winding Magnetless Vernier Reluctance Linear Machine in Long-Stroke Module

Zhenghao Li, Shuangxia Niu, Senior Member, IEEE, Mingyuan Jiang, Zekai Lyu, Member, IEEE, Wei Liu, Senior Member, IEEE, and *KT Chau, Fellow, IEEE*

***Abstract*— Vernier reluctance linear machines (VRLM), taking advantage of controllable magnetic field, simple structure and low consumption of rare-earth material, are promising actuators for long stroke applications in industrial processing field. However, due to the limited excitation, this machine exhibits limited force density with redundant field winding, which hinders its wider application. Aiming to eliminate DC coils, simplify manufacturing process and strengthen its load capacity, an integrated toroidal winding design excited by zero-sequence current is proposed for Vernier reluctance linear machine in this paper. The key is to compare different arrangements of excitations to boost the contents of working harmonics, make better use of modulated harmonics and select a proper gear ratio. Driven by integrated toroidal winding, the slot utilization of VRLM is improved, and the manufacturing process of the machine is significantly simplified. In this paper, winding arrangements of VRLM and its working mechanism are analyzed, along with some design guidelines, including slot-pole combinations, geometric dimensions, etc. Finally, the prototype is built for performance evaluation and experimental verification.**

***Index Terms*—Long Stroke Application, Integrated Toroidal Winding, Vernier Reluctance Linear Machine**

I. INTRODUCTION

LINEAR machines, which remove the gearbox and other kinetic energy transmission devices, take advantage of high acceleration, high reliability and low mechanical loss, and have been widely used in various direct-drive applications, such as railway transportation and industrial assembly line scenarios [1-2]. In the realm of industrial processing applications, the permanent magnet synchronous linear machine (PMSLM) has emerged as a dominant linear machine, leveraging advancements in magnetic materials to offer higher force density and dynamic response. However, for long stroke applications, the PMSLM faces cost and maintenance complexity issues, with fault demagnetization posing additional challenges [3]. Over the past decade, induction linear machines (ILM) have served as actuators for long stroke applications, albeit with drawbacks like low efficiency and power factor due to eddy current effects [4]. Reluctance linear machines (RLM), operating based on airgap reluctance variation, present a promising alternative. Switched reluctance linear machines (SRLM), known for their robust structure and cost-effectiveness, are suitable for long stroke linear applications but exhibit significant thrust ripple due to their commutation driving mode [5]. Therefore, researchers have focused on developing effective electromagnetic designs and specialized control methods to enhance its performance [6-7]. Synchronous reluctance linear machines (Syn-RLM), featuring flux barriers in their secondary to create saliency, offer a control method akin to PMSLM and can mitigate force ripple effectively [8]. Emerging as another candidate, the variable flux reluctance linear machine (VF-RLM) employs additional excitation on the primary part and reluctance variation during mover movement [9]. In spite of flexibility in excitations and simplified control methods, the load capability of VF-RLM still needs to be improved and various design methods have been proposed, such as enhanced excitations with integration of permanent magnets and high-temperature superconducting magnets [10], niche magnetic frameworks with modularized or multitoothed structures [11-13], and optimized winding configurations with improved winding factors [14-15] to boost the force and overload capacity.

In recent years, the magnetic gear (MG) effect, also known as the flux modulation effect, has emerged as a significant method for enhancing output performance in both rotary and linear direct-drive applications [16-17]. The MG effect facilitates the transformation of a magnetic field from high pole pair number and low speed to low pole pair number and high speed, thereby optimizing armature windings' utilization and amplifying output performance [18]. Additionally, the modulation of the static magnetic field generated by stator excitation into a travelling magnetic field induces corresponding voltages for torque/force production [19]. Initially implemented in a dual-PM Vernier reluctance machine (DPM-VRM) [20], the MG effect was swiftly adapted to the variable flux reluctance machine, leading to the creation of the variable flux Vernier reluctance machine (VF-VRM) [21]. An innovative VF-VRM design featuring harmonically modulated MMF was proposed to generate high pole pair number magnetic fields with reduced excitation requirements [22]. While most current VF-VRMs utilize field winding excitation, which presents challenges such as conflicting slot areas and complex manufacturing processes, a novel drive method introduced in a recent study eliminates the need for a field winding by supplying biased sinusoidal current to the armature winding, effectively reducing current losses [23]. This drive technique has been extended to VF-VRM in another study to maximize output torque. Despite these advancements, a comprehensive understanding of the machine's operational principles and the absence of design guidelines still remain as areas requiring further exploration and development [24].

In this study, a novel integrated toroidal winding configuration, excited by zero-sequence current, is proposed for the double-sided Vernier reluctance linear machine (DS-VRLM) to reduce copper loss and enhance output force. Different winding configurations with various pole pair numbers of DC excitations are investigated, and the impact of different harmonics is fully analyzed. The paper is structured as follows: Section II introduces the mechanical structure, winding configuration, and drive circuit, with harmonic

Z. Li, S. Niu, M. Jiang, Z. Lyu, W. Liu and K. T. Chau are with the Department of Electrical and Electronic Engineering, The Hong Kong Polytechnic University, Hong Kong SAR, 999077, China.

Corresponding author: Shuangxia Niu. (e-mail: eesxniu@polyu.edu.hk)

analysis for assessing the contributions of different harmonics. Section III establishes the parametric model, analyzes parameter sensitivity, and evaluates output force performance globally using the multi-objective genetic algorithm (MOGA). Section IV comprehensively evaluates the optimized case in terms of rated output force, overload capability, losses, etc. Section V involves fabricating a prototype and conducting experiments to verify the feasibility of the proposed solution. Section VI presents the conclusions drawn from the research.

II. Operation Principle

A. Machine Structure and Integrated Toroidal Winding (ITW) Configurations

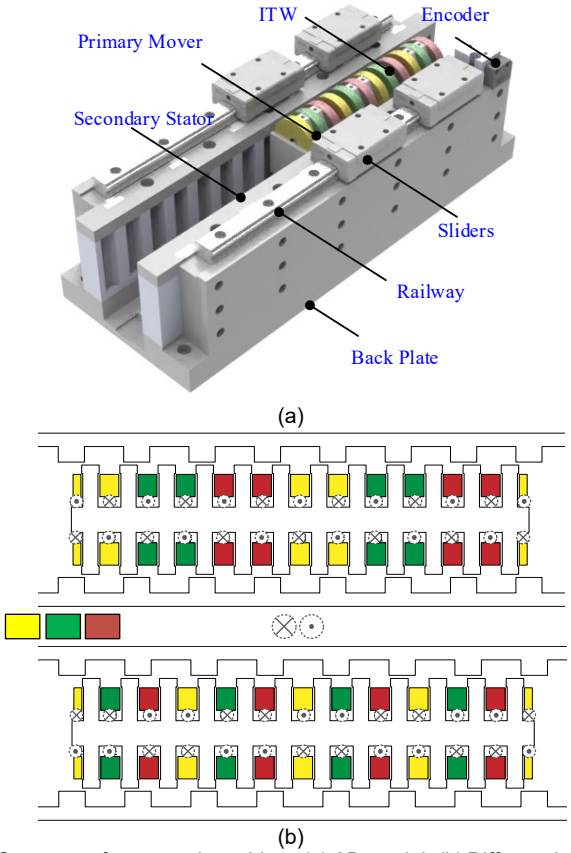

Fig. 1. Structure of proposed machine. *(a) 3D model. (b)* Different integrated toroidal winding design.

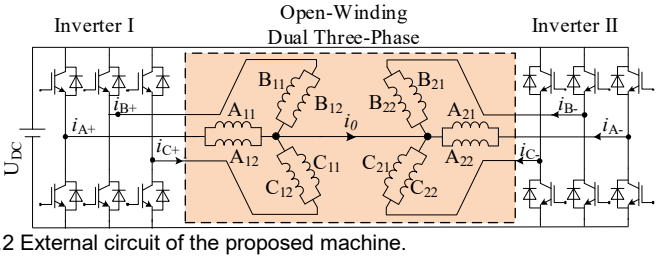

Fig.2 External circuit of the proposed machine.

Fig. 1(a) illustrates a 3D model of the proposed double-sided Vernier reluctance linear machine (DS-VRLM) equipped with integrated toroidal winding (ITW or ITW-VRLM). This machine features a double-sided structure with the ITW wound on its yoke. The secondary part incorporates double-side salient-pole teeth symmetrically positioned on both sides of the mover. Fig. 1(b) represents two winding configurations of different pole pair numbers of DC components. As shown in Fig. 1(b), the DC component of the winding current can be equivalently represented as different virtual windings, and the proposed ITWs can be classified into different phases accordingly. Compared to the machine with separated armature and field winding, the integrated winding could optimize the use of insulation space and improve the effective slot area. Furthermore, the proposed toroidal windings effectively shorten the end length and guarantee the winding factor of it. Fig. 2 displays the external circuit of the proposed machine. In this configuration, the windings, adopting an open-winding dual three-phase (OW-DTP) layout, utilize zero-sequence currents for excitation. The whole system employs two full-bridge inverters sharing a common DC bus.

B. Harmonic Analysis and Back EMF of ITW

Currents in winding 1 and winding 2 in the same phase have the same phasor for the AC component but opposite polarities for the DC part. According to the winding configuration and drive circuit in Fig. 1(b), the current can be expressed as follows,

$$\begin{cases} i_{A1}(t) = I_{ac}\sin(\omega_e\, t + \theta_e) + I_{dc} \\ i_{A2}(t) = I_{ac}\sin(\omega_e\, t + \theta_e) - I_{dc} \\ i_{B1}(t) = I_{ac}\sin\left(\omega_e\, t + \theta_e - \frac{2\pi}{3}\right) + I_{dc} \\ i_{B2}(t) = I_{ac}\sin\left(\omega_e\, t + \theta_e - \frac{2\pi}{3}\right) - I_{dc} \\ i_{C1}(t) = I_{ac}\sin\left(\omega_e\, t + \theta_e + \frac{2\pi}{3}\right) + I_{dc} \\ i_{C2}(t) = I_{ac}\sin\left(\omega_e\, t + \theta_e + \frac{2\pi}{3}\right) - I_{dc} \end{cases} \quad (1)$$

where I_{ac} is the amplitude of AC component, and I_{dc} is the value of DC component. Fig. 1(b) presents the distribution of DC and AC components with different winding arrangements. In the first figure of Fig. 1(b), the number of mover slots per pole pair Q_{dc} is set as 2, and the pole-pair number (PPN) of DC component P_{dc} equals to 6, when the number of mover slots N_m=12. In the second figure of Fig. 1(b), Q_{dc} is set as 4, and the PPN of DC component P_{dc} equals to 3. The pole pitch of DC component τ_{dc} can be expressed as,

$$\tau_{dc} = \frac{N_m}{P_{dc}}\tau_m = Q_{dc}\tau_m \quad (2)$$

where τ_m is the pole pitch of the mover teeth.

The MMF of DC excitation can be expressed as equation (3).

$$\begin{cases} F_{dc}(x) = \sum_{h=1,3,5\ldots} \frac{4F_{max1}}{h\pi}\sin\left(h\frac{\pi}{\tau_{dc}}x + \theta_h\right) \\ F_{max1} = N_{coil}I_{dc} \end{cases} \quad (3)$$

where F_{max1} is the maximum value of DC MMF, θ_h is the initial phase of DC excitation, and N_{coil} is the number of coil per slot.

The MMF of DC excitation $F_{dc}(x)$ is firstly modulated by mover teeth, where normalized permeance function $\Lambda_m(x)$ can be expressed as follows,

$$\begin{cases} \Lambda_m(x) = \Lambda_{m(0)} + \sum_{n1=1,2,3\ldots}\Lambda_{m(n1)}\cos\left(n_1\frac{\pi}{\tau_m}x + \theta_{n1}\right) \\ \Lambda_{m(0)} = 2\frac{x_1}{\tau_m}\left(\Lambda_{s(max)} - \Lambda_{s(min)}\right) \\ \Lambda_{m(n1)} = \frac{2}{n_1\pi}\Lambda_m\sin\left(n_1\frac{\pi}{\tau_m}x_1\right) \end{cases} \quad (4)$$

where $\Lambda_{m(n1)}$ is the amplitude of n_1th harmonics of mover permeance function, x_2 is the width of mover slot, $\Lambda_{m(min)}$ and $\Lambda_{m(max)}$ is the minimum and the maximum value of mover permeance, respectively. Modulated by the mover teeth, the MMF of DC excitation is modified, denoted as $F'_{dc}(x)$, which can be calculated as follows, by substituting (2)(3)(4) into (5) and shown in Fig. 3(a),

$$F'_{dc}(x) = F_{dc}(x)\cdot\Lambda_m(x) \quad (5)$$

$$= \left[\sum_{h=1,3,5\ldots} \frac{4F_{\max 1}}{h\pi} \sin\left(h\frac{\pi}{\tau_{dc}}x + \theta_h\right)\right] \cdot$$
$$\left[\Lambda_{m(0)} + \sum_{n_1=1,2,3\ldots} \Lambda_{m(n1)} \cos\left(n_1\frac{\pi}{\tau_m}x + \theta_{n1}\right)\right]$$
$$= \left\{\sum_{h=1,3,5\ldots}\sum_{n_1=0,1,2\ldots}\left[\frac{2F_{\max 1}}{h\pi}\Lambda_{m(n1)}\sin\left((h \pm Q_{dc}\, n_1)\frac{\pi}{\tau_{dc}}\, x + \theta_h + \theta_{n1}\right)\right]\right\}$$

Furthermore, the proposed VRLM are designed to utilize DC harmonics in (6),

$$P'_{dc} = |h \pm Q_{dc} n_1| P_{dc} \tag{6}$$

when Q_{dc}=2j, indicating that DC excitation switches its polarity every j slots, DC component mainly composed of fundamental and $|h \pm 2jn_1|$ harmonics in the air gap.

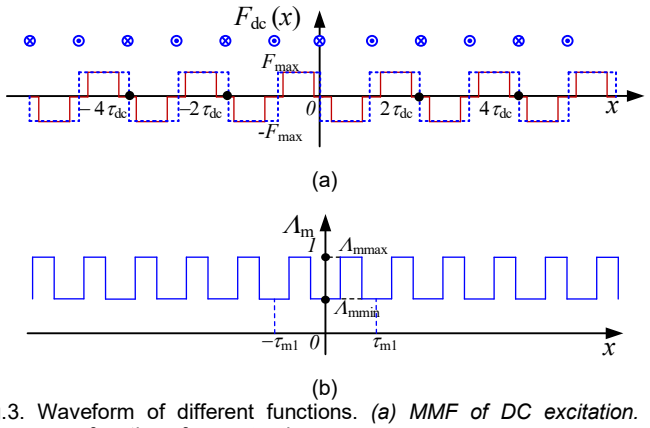

Fig.3. Waveform of different functions. *(a) MMF of DC excitation. (b) Permeance function of* stator teeth.

The MMF of $F_{dc}(x)$ is then modulated by stator teeth to generate flux density $B(h', n_2)$, whose stator permeance function $\Lambda_s(x,t)$ can be expressed as following (7), and shown in Fig. 3(b),

$$\begin{cases} \Lambda_s(x,t) = \Lambda_{s(0)} + \sum_{n2=1,2,3\ldots} \Lambda_{s(n2)} \cos\left[n_2\frac{\pi}{\tau_s}(x + v_m t) + \theta_{n2}\right] \\ \Lambda_{s(0)} = 2\frac{\Lambda_{s(\max)} - \Lambda_{s(\min)}}{\tau_s} x_2 \\ \Lambda_{s(n_2)} = \frac{2}{n2\cdot\pi}\Lambda_s \sin\left(n_2\frac{\pi}{\tau_s}x_2\right) \end{cases} \tag{7}$$

where $\Lambda_{s(n2)}$ is the amplitude of n_2th harmonics of stator permeance function, τ_s is the pole pitch of the stator teeth, x_2 is the width of stator slot, $\Lambda_{s(min)}$ and $\Lambda_{s(max)}$ is the minimum and the maximum value of stator permeance, respectively.

Then the flux density of DC excitation can be calculated as (8),

$$B_{(h,n1,n2)}(x,t) = F'_{dc}(x) \cdot \Lambda_s(x,t) \tag{8}$$
$$= \sum_{h=1,3,5\ldots}\sum_{n1=0,1,2\ldots}\frac{2F_{max}}{h\pi}\sin\left((h \pm 4n_1)\frac{\pi}{\tau_{dc}}\, x\right) \cdot \Lambda_{m_{n1}}$$
$$\cdot \sum_{n_2=1,2,3\ldots} \Lambda_{s0} + \Lambda_{s_{n2}} \cos\left[\frac{n_2\pi}{\tau_s}(x + v_m t)\right]$$
$$= \sum_{n_2=0,1,2\ldots}\sum_{h=1,3,5\ldots}\sum_{n1=0,1,2\ldots}\frac{F_{max}}{h\pi}\Lambda_{m_{n_1}}\Lambda_{s_{n_2}}$$
$$\cdot \sin\left\{\frac{\pi}{L_{m1}}\left[\left((h \pm 4n_1)P_{dc} \pm n_2 N_s\right)\left(x + \frac{n_2 N_s}{(h\pm 4n_1)P_{dc}\pm n_2 N_s} v_m t\right)\right]\right.$$

The EMF calculation of the proposed integrated toroidal winding can be expressed as follows,

$$e_m(t) = -\frac{d\psi_m(t)}{dt} = 2l_{stk}B_{(h,n1,n2)}k_{wn}\frac{\tau_{ac}}{\tau_s}\, v_m \sin\left(n_2\frac{\pi}{\tau_s}v_m t\right) \tag{9}$$

When the current of the motor is fixed, Back EMF represents the capability of motor's output force and power conversion directly. In (9), it can be clearly seen that back EMF is proportional to the winding factor and τ_{ac} and is inversely proportional to τ_s.

In flux modulation theory, the ratio between pole pitch of stator salient teeth and pole pitch of working harmonics of AC components is defined as gear ratio G_r, which can also be defined as be ratio between the number of stator teeth aligning with mover N_s, and pole pair number of AC components, P_{ac}. Gear ratio G_r directly indicates the amplification factor of the motor's back EMF.

$$G_r = \frac{\tau_{ac}}{\tau_s} = \frac{N_s}{P_{ac}} \tag{10}$$

To further demonstrate the advantages of the proposed winding configuration, the resulted EMF amplitudes in one turn per phase of proposed Winding and VF-RLM, whose topology is shown in Fig. 16 in the following Section IV C, are compared. The calculation is conducted under conditions shown in TABLE I and the results are summarized in TABLE II. As shown in TABLE II, the proposed winding configuration achieves higher EMF amplitudes in one turn per phase. Compared to the conventional VF-RLM with conventional double layer concentrated winding (DL-CW) proposed in the existing work [9], the proposed winding configuration could achieve higher winding factor, gear ratio of the working harmonic and resultant back EMF.

TABLE I
INITIAL DESIGN PARAMETER AND DESIGN SPECIFICATION

Symbol	Parameter	Unit	Value
H_{total}	*Total length along Y-axis*	mm	80
k_{sp}	*Split ratio*	-	0.7
k_{dc}	*DC loss ratio*	-	0.6
h_{mt}	*Height of mover teeth*	mm	30
h_{st}	*Height of stator teeth*	mm	6.5
L_m	*Mover length*	mm	210
k_{st}	*Ratio of stator teeth width*	-	0.35
N_{coil}	*Number of coils of ITW*	-	75
P_{loss}	*Total copper loss*	W	120
v_m	*Velocity*	m/s	1
$L_{m(max)}$	*Max loading*	kg	20
$A_{m(max)}$	*Max acceleration*	m/s2	4
M_m	*Mover mass*	kg	5
$v_{m(max)}$	*Max velocity*	m/s	10
$f_{t(con)}$	*Continuous force*	N	100
$f_{t(pk)}$	*Peak thrust force*	N	180
$P_{(pk)}$	*Peak power capacity*	kW	1

C. Electromagnetic Force Calculation

The winding function $N_a(x)$ is defined as the MMF of one phase armature winding at unit current when the origin point is aligned with the middle point of the armature winding slot, which can be expressed by (11),

$$N_a(x) = \sum_{j=1,3,5\ldots}\frac{2}{k\pi}\frac{1}{P_{ac}}N_{coil}k_{w,k}\sin\left(k\frac{\pi}{\tau_{ac}}x\right) \tag{11}$$

where k is the order of the armature winding function harmonics, P_{ac} is the fundamental *PPN* of armature winding equaling to N_m/mQ_{ac}, and Q_{ac} is the number of mover slots per pole pair per phase. $k_{w,k}$ is the winding factor of the kth order harmonics, and τ_{ac} is the pole pitch of armature winding. Accordingly, the MMF of armature excitation $F_{ac}(x,t)$ can be determined and the is illustrated in Fig. 4, where the MMF of armature excitation with/without mover teeth modulation is shown as red solid/blue dash line. The MMFs of AC component in each phase are expressed as follows,

$$\begin{cases} F_a(x,t) = \sum_{k=1,3,5\ldots}\frac{4F_{max2}}{k\pi}\sin\left(\frac{k\pi}{\tau_{ac}}x + \theta_k\right)\cos(\omega_e t) \\ F_b(x,t) = \sum_{k=1,3,5\ldots}\frac{4F_{max2}}{k\pi}\sin\left(\frac{k\pi}{\tau_{ac}}x + \theta_k\right)\cos\left(\omega_e t - \frac{2\pi}{3}\right) \\ F_c(x,t) = \sum_{k=1,3,5\ldots}\frac{4F_{max2}}{k\pi}\sin\left(\frac{k\pi}{\tau_{ac}}x + \theta_k\right)\cos\left(\omega_e t + \frac{2\pi}{3}\right) \end{cases} \tag{12}$$

where F_{max2} is the maximum value of armature MMF, θ_k is the initial phase of armature excitation, and N_{coil} is the number of turns per coil. The armature MMF as a whole are calculated by the sum of MMF in each phase, which is shown as follows,

$$\begin{cases} F_{ac}(x,t) = F_a(x,t) + F_b(x,t) + F_c(x,t) \\ = \sum_{k=1,3,5\ldots} \frac{6F_{max2}}{k\pi} \sin\left[k\frac{\pi}{\tau_{ac}}x + \omega_e t + \theta_k\right] \\ F_{max2} = k_{w,k}N_{coil}I_{ac}, \tau_{ac} = \frac{N_s}{P_{ac}}\tau_s \end{cases} \quad (13)$$

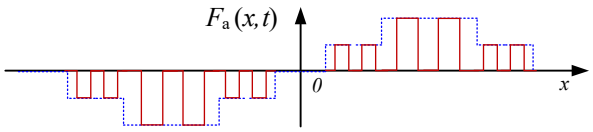

Fig.4. MMF of AC excitation.

The MMF of $F_{dc}(x)$ and $F_{ac}(x,t)$ is then modulated by stator teeth to generate electromagnetic force, The electromagnetic force is determined by the key components of harmonics mentioned above. According to the flux modulation theory, the electromagnetic force of the proposed machine produced by interaction between ac and DC components can be calculated by following equation,

$$f_e(t) = L_{stk}\int_0^{L_m} \Lambda_s(x,t)\, dF'_{dc}(x) F_{ac}(x,t) \quad (14)$$

where L_{stk} is the stack length of machine and L_m is the length of the mover. Substituting (4), (7) and (13) into (14), the force generated by AC and DC components can be further deduced as follows,

$$\begin{aligned} f_e(t) &= \frac{1}{2}L_{stk}\Lambda_{s(n2)}F'_{dc(h')}F_{ac(k)}\int_0^{L_m}\cos\left[n_2\frac{\pi}{\tau_s}(x+v_m t)+\theta_{n2}\right] \\ &\cdot\left(h'\frac{\pi}{\tau_{dc}} \pm k\frac{\pi}{\tau_{ac}}\right)\sin\left[\left(h'\frac{\pi}{\tau_{dc}} \pm k\frac{\pi}{\tau_{ac}}\right)x + \omega_e t + \theta_k \pm \theta_{h'}\right]\cdot dx \\ &= \frac{1}{2}L_{stk}\Lambda_{s(n2)}F'_{dc(h')}F_{ac(k)}\cdot\left(h'\frac{\pi}{\tau_{dc}} \pm k\frac{\pi}{\tau_{ac}}\right)\cdot\left[\pm\frac{1}{2}\int_0^{L_m}\sin\right. \\ &\left.\left(\left(\frac{n_2\pi}{\tau_s} \pm \frac{h'\pi}{\tau_{dc}} \pm \frac{k\pi}{\tau_{ac}}\right)x + \left(\frac{n_2\pi}{\tau_s}v_m \pm \omega_e\right)t + \theta_k \pm \theta_{h'} \pm \theta_{n2}\right)\cdot dx\right] \end{aligned} \quad (15)$$

According to (15), the electromagnetic force $f_e(t)$ can be generated when the following condition can be satisfied.

$$n_2\frac{\pi}{\tau_s} \pm h'\frac{\pi}{\tau_{dc}} \pm k\frac{\pi}{\tau_{ac}} = n_2N_s \pm h'P_{dc} \pm kP_{ac} = 0 \quad (16)$$

Furtherly, the electromagnetic force $f_e(t)$ can be divided into average force f_{avg} and force ripple $f_{rip}(t)$, which are listed in (17). It should be noticed that the average force is proportional to the number of stator teeth, fundamental component of stator permeance, and amplitudes of MMF of DC and AC component.

$$\begin{cases} f_{avg} = \frac{\pi}{2}N_sL_{stk}\Lambda_{s(1)}\sum_{h',k}\left[F_{dc(h')}F_{ac(k)}\sin\left(\theta_k \pm \theta_{h'} - \theta_{s(1)}\right)\right], \\ when\ \frac{n_2\pi}{\tau_s}v_m \pm \omega_e = 0 \\ f_{rip}(t) = \pm\frac{n_2\pi}{2}N_sL_{stk}\Lambda_{s(n2)}\sum_{h',k}\left[F'_{dc(h')}F_{ac(k)}\cdot\sin\right. \\ \left.\left(\left(\frac{n_2\pi}{\tau_s}v_m \pm \omega_e\right)t + \theta_k \pm \theta_{h'} \pm \theta_{s(n2)}\right)\right], when\ \frac{n_2\pi}{\tau_s}v_m \pm \omega_e \neq 0 \end{cases} \quad (17)$$

D. Force Contributions of Working Harmonics

The design parameters of the machines are defined in Fig.5, and the values of the parameters are set in TABLE I for fair comparison. As shown in Fig. 1(b), variable DC arrangements can be designed for the proposed winding configuration with Q_{dc} set as 2 and 4 for discussion, and the waveforms of the DC MMF of two arrangements are shown in Fig. 6. As shown in Fig.6, P_{dc} can be set as 6 or 3 in the proposed machine with 12 mover slots, and some other harmonics also exist after mover teeth modulation, whose *PPN* can be calculated by (6). *PPN* of armature harmonics can be calculated using (16).

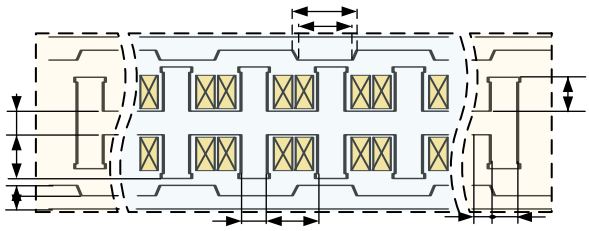

Fig.5. Geometric parameters of DS-VRLM.

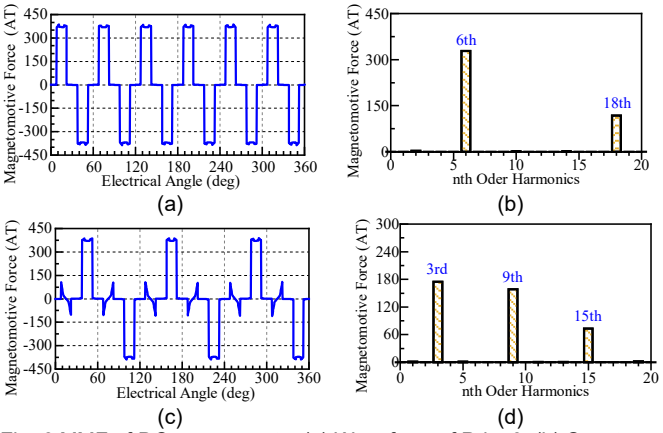

Fig. 6 MMF of DC components. (a) Waveform of Pdc=6. (b) Spectrum of Pdc=6. (c) Waveform of Pdc=3. (b) Spectrum of Pdc=3.

TABLE III
FORCE COMPARISON OF INTEGRATED TOROIDAL WINDINGS

N_s	P_{ac}	G_r	Force Prop. (%)	Total Force	Force Rip.
Q_{dc}=2, P_{dc}=6, P'_{dc}=18					
7	1	7.00	60.00	**76.40**	**7.89**
	13	0.54	22.48		
	11	0.64	20.12		
	25	0.28	-4.00		
8	2	4.00	55.57	66.50	135.50
	14	0.57	26.57		
	10	0.80	16.93		
	26	0.31	-1.90		
10	4	2.50	60.44	39.20	14.10
	16	0.625	22.76		
	8	1.25	20.33		
	28	0.36	-4.02		
11	5	2.20	60.38	32.80	43.39
	17	0.65	22.60		
	7	1.57	21.06		
	29	0.38	-3.79		
Q_{dc}=2, P_{dc}=3, P'_{dc}=9					
N_s	P_{ac}	G_r	Force Prop. (%)	Total Force	Force Rip.
7	4	1.75	0	**52.90**	**23.43**
	10	0.70	42.45		
	2	3.50	44.71		
	16	0.44	0		
8	5	1.60	7.84	75.79	115.00
	11	0.73	38.00		
	1	8.00	37.46		
	17	0.47	3.40		
10	7	1.43	17.75	81.72	201.80
	13	0.77	17.10		
	1	10.00	46.55		
	19	0.53	6.07		
11	8	1.38	30.00	59.37	14.59
	14	0.79	0		
	2	5.50	60.27		

TABLE II
INDUCED VOLTAGE COMPARISON OF PROPOSED ITW WINDING AND VF-RLM [9]

	P_{dc}	N_s	(h', n_2)	P_w	τ_{ac}	τ_s	G_r	$B(h', n_2)$ (T)	k_p	k_d	E_{ph1}(*) (mV/Turns)	ΣE_{ph1} (mV/Turns)	FEA (mV/Turns)	Cal. Error (%)
ITW-VRLM	3	7	(1, -1)	4	26.25	15	1.75	0.068	0.00	1.00	0.00	73.0	69.0	5.8
			(3, -1)	2	52.50	15	3.5	0.040	1.00	1.00	56.16			
			(5, -1)	8	13.13	15	0.88	0.017	0.00	1.00	0.00			
			(1, 1)	10	7.50	15	0.5	0.0011	1.00	1.00	18.51			
			(3, 1)	16	5.25	15	0.35	0.0064	0.00	1.00	0.00			
			(5, 1)	22	4.04	15	0.27	0.0053	-1.00	1.00	-2.02			
	6	7	(1, -1)	1	105	15	7	0.054	1.00	0.966	147.14	137.7	141.9	3.0
			(3, -1)	11	9.55	15	0.64	0.0086	-1.00	-0.966	2.12			
			(5, -1)	23	4.57	15	0.30	0.0072	-1.00	0.966	-0.84			
			(1, 1)	13	8.08	15	0.54	0.052	-1.00	-0.966	0.14			
			(3, 1)	25	4.20	15	0.28	0.0065	-1.00	0.966	-0.15			
			(5, 1)	37	2.84	15	0.19	0.0061	-1.00	-0.966	0.04			
VF-RLM	6	10	(1, -1)	4	26.25	10.5	2.50	0.058	0.866	1.00	50.32	41.1	39.0	5.4
			(3, -1)	8	13.13	10.5	1.25	0.00021	0.866	1.00	0.089			
			(5, -1)	20	5.25	10.5	0.50	0.057	-0.866	1.00	-9.83			
			(1, 1)	16	6.56	10.5	0.31	0.0068	-0.866	1.00	-0.28			
			(3, 1)	28	3.75	10.5	0.63	0.0013	0.866	1.00	0.38			
			(5, 1)	40	2.63	10.5	0.36	0.0030	-0.866	1.00	-0.51			
	6	11	(1, -1)	5	21.00	9.55	2.20	0.054	0.966	0.966	44.44	35.8	37.7	5.0
			(3, -1)	7	15.00	9.55	1.57	0.0045	0.966	0.966	2.63			
			(5, -1)	19	5.53	9.55	0.58	0.053	-0.966	0.966	-11.47			
			(1, 1)	17	6.20	9.55	0.35	0.0081	0.966	0.966	1.078			
			(3, 1)	29	3.62	9.55	0.65	0.0022	-0.966	0.966	-0.53			
			(5, 1)	41	2.56	9.55	0.38	0.0011	0.966	0.966	0.16			

	20	0.55	0	

The output force of various winding arrangements with feasible slot/pole combinations is calculated using equation (17), and the results are summarized in TABLE III. Specifically, for the proposed machine with N_m=12 and N_s=7, a higher output force and lower force ripple are achieved with P_{dc}=6 compared to the P_{dc}=3 scenario. The average force in the P_{dc}=3 scenario increases due to the higher gear ratio, notably for machines with N_s=8 and 10. However, significant force ripples occur in these machines due to uneliminated even-order harmonics in the flux. In the P_{dc}=6 scenario, with a further increase in the number of poles, the advantage of ITW becomes less apparent due to the reduced gear ratio. Considering overall force performance, machines with N_m=12 and N_s=7 exhibit higher thrust force and lower ripple. To be noticed, the end effect is neglected for clearance of the harmonic contribution illustration in this part. Therefore, the conclusion of this part is also suitable for rotary counterpart.

Taking machines with N_m=12 and N_s=7 as an example, the amplitudes, speeds, phase angles, and force contributions of different harmonics are detailed in TABLE III, with output force calculated using (17). Analysis from TABLE IV and V reveals that the configuration with P_{dc}=6, P_{ac}=1, N_s=7 can achieve 60% of the total force through force contributions. In the case of P_{dc}=3 machines, configurations P_{dc}=3, P_{ac}=10, N_s=7, and P_{dc}=9, P_{ac}=2, N_s=7 yield 42.46% and 44.73% of the total force.

III. DESIGN MECHANISM GUIDELINES

A. Parametric Sensitivity Analysis

Machine with P_{dc}=6, N_s=7, which exhibits the best output force performance based on the previous analysis, is studied in this part. The initial parameters of the machine are listed in TABLE I.

Some key parameters are pre-defined in this part, including **split ratio k_{sp}**, **DC loss ratio, k_{dc}**, etc.

Split ratio k_{sp}, which reflects the ratio between the mover height and total height, is defined as follows,

$$k_{sp} = \frac{h_m}{H_{total}} \tag{18}$$

where h_m is the height of mover part, H_{total} is the height of the total machine, which is fixed to 80mm in this paper.

DC loss ratio is defined as the ratio between DC excitation loss and the total copper loss, which can be expressed as follows,

$$\begin{cases} k_{dc} = \dfrac{p_{dc}}{p_{loss}} \\ I_{dc} = \sqrt{k_{dc}} I_{rms} \\ I_{ac} = \sqrt{2} \cdot \sqrt{1 - k_{dc}} I_{rms} \end{cases} \tag{19}$$

where p_{dc} is the copper loss of DC excitation, p_{loss} is the total copper loss of the machine, I_{rms} is the RMS value of phase current.

Fig. 7 investigates the influence of split ratio k_{sp} and stator yoke height h_{sy} on the average output thrust and force ripple ratio. According to Fig. 7(a), when the mover yoke height increases from 4mm to 16mm, the output thrust also increases, as the saturation in the yoke is relieved. However, when the yoke height increases further, the space for the integrated winding is suppressed, which decreases the output thrust. In addition, the optimized value of split ratio k_{sp} is around 0.65. When k_{sp} is lower than this value, the increase of split ratio could bring the increase of average thrust force because of the expansion of space for mover component. However, when the parameters continue to increase, the output thrust force will inevitably decrease because of the saturation problem in the stator yoke. Fig. 7(b) illustrates the impact of above two parameters on the force ripple, which shows that h_{sy}=8mm, k_{sp}=0.65 is considered to be an optimized result.

Fig.8 indicates the influence of DC power loss ratio k_{dc}. The optimal value of k_{dc} is approximately 0.7, at which point the amplitudes of the MMF for both AC and DC excitation are essentially equal.

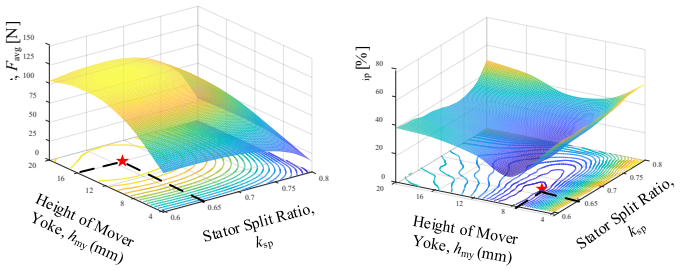

(a) (b)

Fig.7 Thrust force performances v.s. h_{my} and k_{sp}. *(a) Average thrust force. (b) Thrust force ripple ratio.*

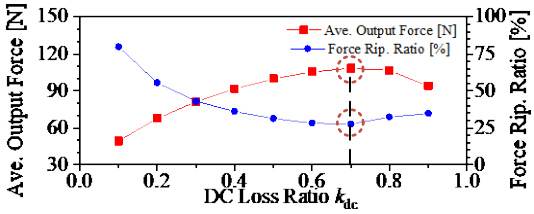

Fig. 8. Thrust force performances v.s. DC loss ratio.

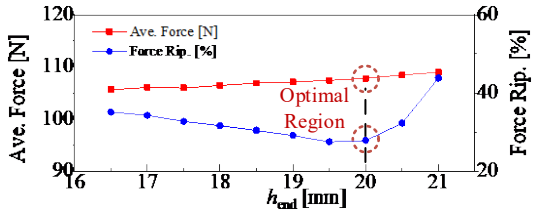

(a)

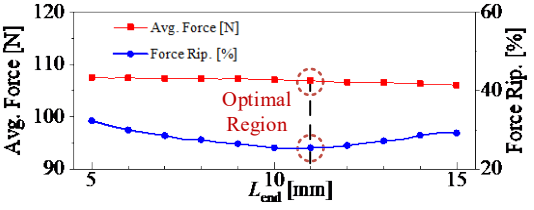

(b)

Fig.9. Influence of the parameters of auxiliary teeth. (a) $h_{end.}$ (b) L_{end}

To relieve the end effect, the extra auxiliary teeth are added at the front and back end of the proposed machine, as shown in Fig. 5. The length and height of the extra teeth, L_{end} and h_{end}, are used to depict the dimensions of the extra teeth. In Fig. 9(a), it can be found that as h_{end} increases, the output thrust increases as well, which is attributed to the decrease of effective air-gap length. However, when h_{end} continues to increase over 20mm, the thrust ripple of the machine increases rapidly because of the distortion of the magnetic field at the end of the machine. According to Fig. 9(b), when the length of end teeth increases, the thrust force initially increases and then decreases because of the amplification of magnetic reluctance.

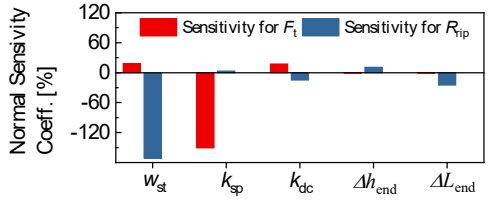

Fig.10. Sensitivity analysis of the different parameters.

To investigate the extent of influence that parameters have on the objective function and to mitigate the impact of manufacturing and installation errors, the sensitivity analysis of above different parameters should be quantitatively analyzed. The normalized sensitivity coefficient S_o can be calculated as,

$$S_o(x_j) = \frac{x_{j0}}{o(x_{j0})}\frac{\partial o}{\partial x_j}\bigg|_{x_j=x_{j0}} = \frac{\Delta o}{o(x_{j0})} \Big/ \frac{\Delta x_j}{x_{j0}} \qquad (20)$$

where x_j is the design variable, x_{j0} is its initial value and Δx_j is the differential change of the design variable. $O(x_{jo})$ is the optimization objective under the initial design parameter [25]. Take the machine with P_{dc}=6, N_s=7, proposed as an example, the sensitivity of the variables, including, k_{sp}, k_{dc}, w_{st} Δh_{end} and Δl_{end}, are calculated in Fig.10. As shown in Fig. 10, the parameter w_{st} significantly influences the force ripple, and the sensitivity coefficient $S_o(w_{st})$ can be calculated as 171.2% at the initial value of 10.5mm. The parameter k_{sp} has great impact on the average force, whose sensitivity coefficient $S_o(k_{sp})$ has reached 150.8%. The DC loss ratio, k_{dc}, exhibits a similar level of sensitivity to both the average thrust force and the force ripple, with calculated sensitivity values of 17.4% and 14.8%, respectively.

B. Global Optimization

In this section, proposed VRLMs with N_s=7, which exhibit relatively better thrust force performance, are optimized in detail furtherly. The motor is optimized under the same copper loss (180W), volume (0.84L), length of air gap (1mm), filling factor F_f (0.4), etc., which are listed in TABLE VI. The parameters of the proposed VRLM with ITW, including k_{sp}, k_{dc}, w_{st}, k_{sm}, h_{end} and L_{end}, are optimized globally via MOGA. The optimization method used in this paper combined the MOGA with finite element method to search the optimal region. The maximum generation is set as 40 with 30 individuals in each generation. The average output thrust force and force ripple ratio are selected as two objective functions.

TABLE VI
FIXED PARAMETERS FOR COMPARISON

Symbol	Parameter	unit	Value
g	*Air-gap length*	mm	1
L_m	*Mover length*	mm	210
H_{total}	*Total length along Y-axis*	mm	80
L_{st}	*Stack Length*	mm	50
P_{loss}	*Total loss of AC and DC currents*	W	180
F_f	*Filling factor*	-	0.45

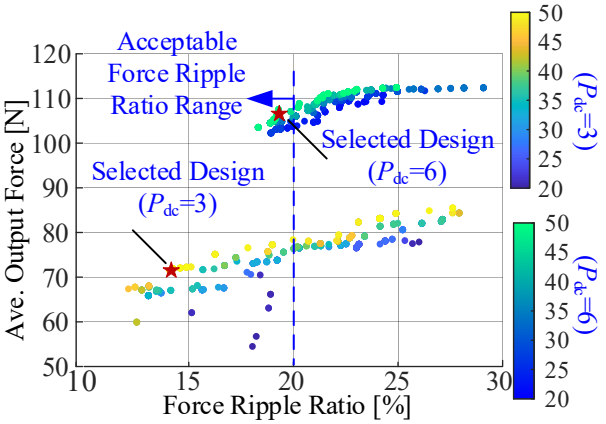

Fig. 11. Optimized Pareto front.

The optimized Pareto Front indicating the optimization results are illustrated in Fig.11. According to optimized Pareto front shown in Fig. 11, thanks to the enhanced gear ratio, machine with P_{dc}=6 design could achieve higher thrust force compared to that with P_{dc}=3 design. However, the latter exhibits lower thrust ripple taking advantages of the weaker end effect. Considering the trade-

TABLE IV
THRUST FORCE CONTRIBUTION OF PROPOSED ITW WINDING WITH P_{DC}=6, P_{AC}=1, N_S=7

N_s	(h', n_2)	P_{dc}	P_{ac}	τ_{ac}	τ_s	F_{dc}	F_{ac}	θ_h	θ_k	θ_{n2}	F_{avg} (Eq.(17))	ΣF_{avg}	FEA
7	(1, -1)	6	1	105.0	15	328.0	138.9	-90.0	0.9	180	46.37	77.2	76.4
	(1, 1)	6	13	8.1		328.0	52.2	-90.0	174.7		17.36		
	(3, -1)	18	11	9.5		118.3	129.6	90.0	175.8		15.56		
	(3, 1)	18	25	4.2		118.3	25.8	90.0	-170.9		-3.07		
	(5, -1)	30	23	4.6		60.8	33.1	90.0	-14.8		-1.98		
	(5, 1)	30	37	2.8		60.8	23.0	90.0	-1.9		1.42		
	(7, -1)	42	35	3.0		57.6	41.1	-90.0	1.4		2.41		
	(7, 1)	42	49	2.1		57.6	15.7	-90.0	8.9		-0.91		
	(9, -1)	54	47	2.2		27.6	26.9	-90.0	172.5		-0.75		
	(9, 1)	54	61	1.7		27.6	18.5	-90.0	-179.4		0.52		
	(11, -1)	66	59	1.8		38.9	18.6	90.0	-175.7		0.74		
	(11, 1)	66	73	1.4		38.9	8.7	90.0	-171.9		-0.34		

TABLE V
THRUST FORCE CONTRIBUTION OF PROPOSED ITW WINDING WITH P_{DC}=3, P_{AC}=2, N_S=7

N_s	(h', n_2)	P'_{dc}	P_{ac}	τ_{ac}	τ_s	F_{dc}	F_{ac}	θ_h	θ_k	θ_{n2}	F_{avg} (Eq.(17))	ΣF_{avg}	FEA
7	(1, -1)	3	4	26.3	15	174.0	0.0	-135.0	-105.3	180	0.00	54.8	52.9
	(1, 1)	3	10	10.5		174.0	217.0	-135.0	126.3		23.27		
	(3, -1)	9	2	52.5		157.6	252.7	-45.0	54.3		24.51		
	(3, 1)	9	16	6.6		157.6	0.0	-45.0	-30.4		0.00		
	(5, -1)	15	8	13.1		72.8	0.0	45.0	-75.8		0.00		
	(5, 1)	15	22	4.8		72.8	50.4	45.0	-48.8		2.28		
	(7, -1)	21	14	7.5		44.2	115.4	135.0	-125.4		3.14		
	(7, 1)	21	28	3.8		44.2	0.0	135.0	163.3		0.00		
	(9, -1)	27	20	5.3		23.0	0.0	45.0	156.9		0.00		
	(9, 1)	27	34	3.1		23.0	61.0	45.0	-56.8		0.86		
	(11, -1)	33	26	4.0		40.3	30.9	135.0	-128.0		0.77		
	(11, 1)	33	40	2.6		40.3	0.0	135.0	132.9		0.00		

off between output thrust force and thrust ripple, the optimized designs are picked up, and parameters are listed in TABLE VII.

TABLE VII
OPTIMIZED PARAMETERS AND PERFORMANCES COMPARISON

	P_{dc}=3	P_{dc}=6
w_{st}, Width of stator teeth (mm)	12.0	11.7
h_{my}, Mover yoke height (mm)	15.0	11.0
h_{sy}, Stator yoke height (mm)	7.1	6.6
h_{end}, End height (mm)	14.0	20.8
L_{end}, End length (mm)	5.9	10.4
w_{end}, End teeth width (mm)	3.8	4.9
k_{sp}, Split ratio	0.70	0.70
k_{dc}, DC loss ratio	0.52	0.68
N_{coil}, Number of ITW per coil	96	110
R_{ph}, Resistance per phase (Ω)	1.07	1.27
i_{dc}, DC component value(A)	5.38	5.66
i_{ac}, AC component amplitude (A)	7.32	5.49
f_t, Rated thrust force (N)(@180W)	71.5	104.5
f_d, Detent force (N) (@Rated I_{dc})	6.48	1.53
R_{rip}, Force ripple ratio (%)	15.1	18.9
D_d, Thrust force density(kN/m^3)	79.5	116.1

IV. ELECTROMAGNETIC PERFORMANCE ANALYSIS

A. Open-Circuit Performances

Fig. 12 and Fig. 13 present the flux linkages of the three phases under different DC excitations. Both machines with P_{dc}=3 and P_{dc}=6 are provided. It can be found that in the machine with P_{dc}=6, the flux linkages are much higher than that with P_{dc}=3, thanks to higher G_r. In the machine with P_{dc}=3, the flux linkages of different phases are balanced. However, the imbalance of magnetic flux will appear due to the end effect in the machine with P_{dc}=6 scenarios.

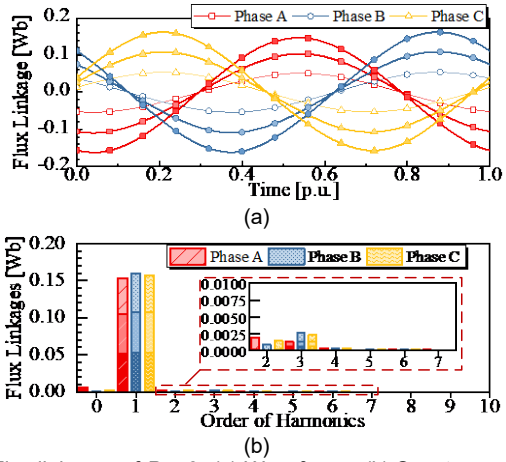

Fig. 12 Flux linkages of P_{dc}=6. *(a) Waveforms. (b) Spectrum*

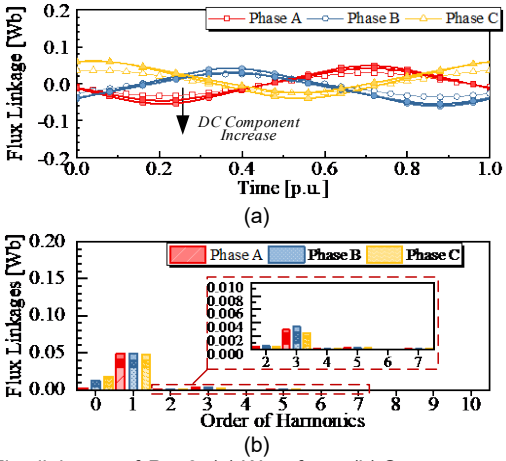

Fig. 13 Flux linkages of P_{dc}=3. (a) Waveform. (b) Spectrum.

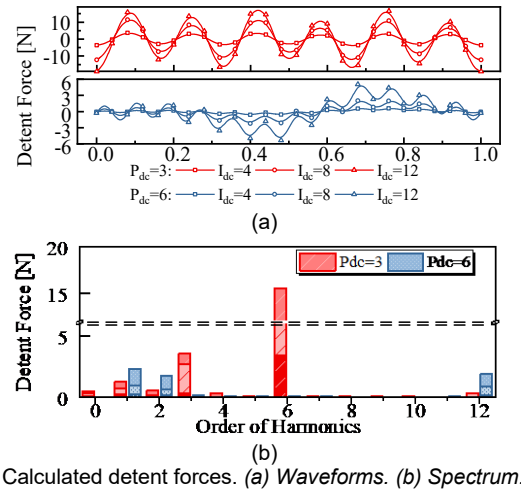

Fig. 14. Calculated detent forces. *(a) Waveforms. (b) Spectrum.*

Fig. 14 compares the detent forces of the different winding configurations. The harmonics of machines with P_{dc}=6 mainly consist of first, second and 12th order harmonics. The first and second order harmonics are caused by end force, and the last component is brought by the cogging force. As the order of DC MMF is 6, the order of cogging force can be calculated via $N_{cog} = \frac{LCM(2P_{dc},N_s)}{N_s}$. For the machine with P_{dc}=3, 6th order harmonic, which is caused by cogging force, accounts for most of the detent force, and the first and third order harmonics caused by end force also exist in the detent force.

B. On-Load Performance Evaluation

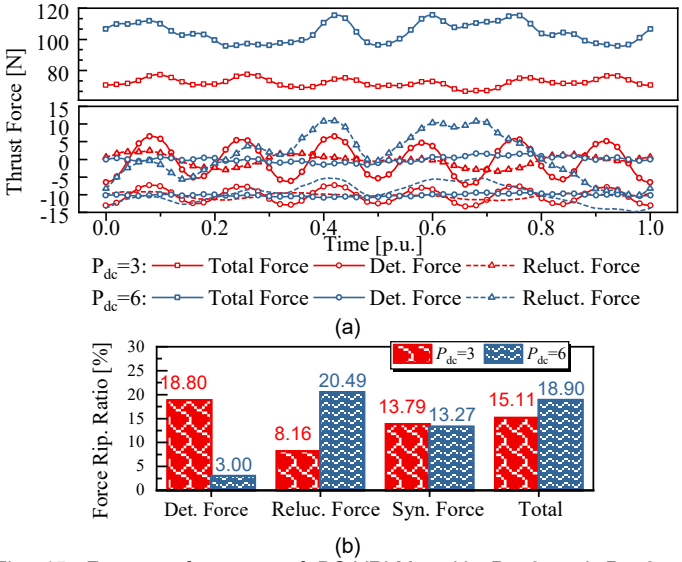

Fig. 15. Force performance of DS-VRLMs with P_{dc}=3 and P_{dc}=6. *(a) Waveforms of force distributions. (b) Force ripple ratio distribution.*

Apart from detent force, the force ripples are caused by different factors, including unbalanced flux linkages (Syn. Force), detent force and unbalanced inductances (Reluc. Force). The force performances of different winding arrangements are depicted in Fig. 15, revealing the force ripple source comparison of two wingding configurations. As shown in Fig. 15(a), the reluctance force ripple caused by imbalanced induction is the main factor, whose peak-to-peak amplitude reached 21.4N in machine with P_{dc}=6. This is primarily attributed to the end effect induced by the excessively low-order working harmonics, which can be mitigated by doubling the slot-pole combination. As for machine with P_{dc}=3, it is obvious that the detent force is the main source of the thrust ripple and causes the 6th order harmonic component, whose peak-to-peak amplitude reached 13.6N. This ripple can be relieved through skewing technology. Fig. 15(b) summarizes the ratio of force ripple sources of the machines quantitatively. As shown in Fig. 15(b), the force ripple of machine with arrangement I (P_{dc} =6) suffered from the reluctance force ripple most, while the arrangement II (P_{dc} =3) is influenced by the detent force. The force ripple caused by unbalanced flux linkages is basically the same. Overall, the force ripple ratio of machine with P_{dc} =3 arrangement is lower than that of the machine with P_{dc} =6 arrangement.

Fig. 16 presents the flux densities of the VRLMs with ITW under the rated operation condition (P_{loss}=180W). By comparison, as shown in Fig. 16(a), proposed VRLM with P_{dc}=6, has lower order harmonics with longer magnetic path, and the mover yoke is more prone to saturate thereafter. However, in the machine with P_{dc}=3, which are 2nd order for 12-7 design, the saturation is much relieved, which can be illustrated in Fig. 16(b).

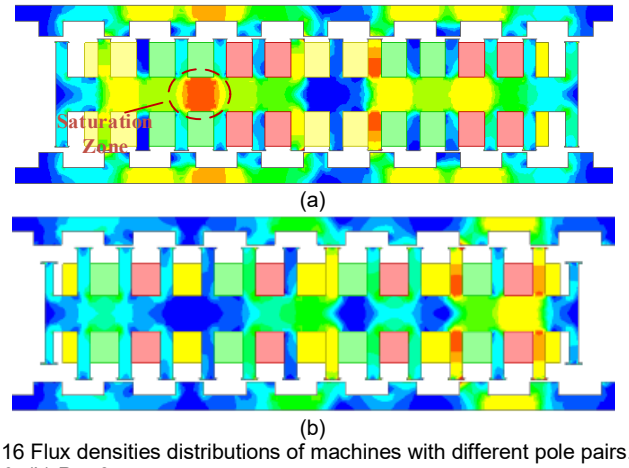

Fig. 16 Flux densities distributions of machines with different pole pairs. *(a) P_{dc}=6. (b) P_{dc}=3.*

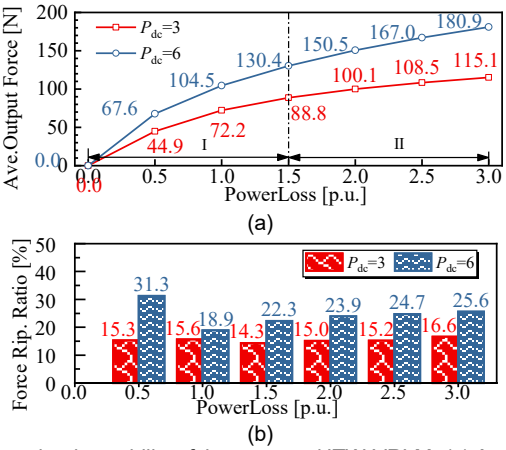

Fig. 17. Over-load capability of the proposed ITW-VRLM. *(a) Average force. (b) Thrust force ripple.*

Fig. 17 illustrates the thrust characteristics of the proposed VRLMs with different winding arrangements (P_{dc} =3 and P_{dc} =6), detailing their average force and force ripple ratio across power losses ranging from 90W to 540W. In Fig. 17(a), the machine with P_{dc} =6 demonstrates higher thrust force compared to the P_{dc} =3 machine, nearing saturation when excitation exceeds 1.5 times the rated condition. Regarding force ripple performance, Fig. 17(b) shows that machines with P_{dc}=6 exhibit higher force ripple, particularly under high loading conditions.

C. Comparative Study

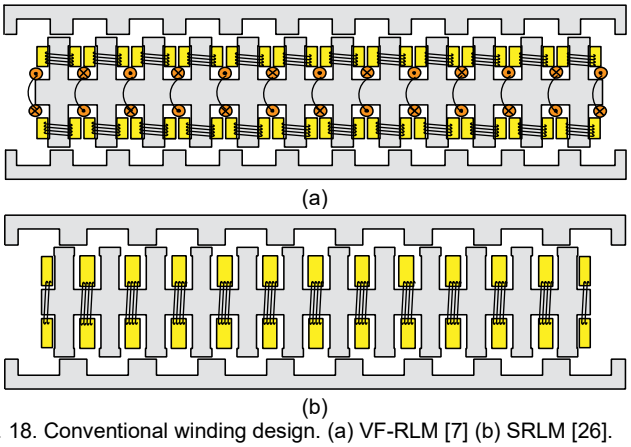

Fig. 18. Conventional winding design. (a) VF-RLM [7] (b) SRLM [26].

To elucidate force performance of the proposed DS-VRLM, a comparative analysis is conducted with two other reluctance linear machines: **Variable Flux Reluctance Linear Machine (VF-RLM)** [7] and **Switched Reluctance Linear Machine (SRLM)** [26][27]. This comparison, conducted under identical input power and dimensions for fairness, showcases the machine topologies in Fig. 18. In Fig. 18(a), the conventional variable flux linear reluctance machine adopts double-layer concentrated winding (DL-CW) and the conventional slot-pole combination of this motor is selected as 12s10p. The winding factors of this machine are calculated as 0.866. Fig. 18(b) illustrates the SRLM, employing single-layer toroidal winding and bipolar square-wave excitation is applied to this motor [27].

TABLE VIII
DESIGN PARAMETERS AND PERFORMANCES COMPARISONS

	VF-RLM	SRLM	Proposed
L_m, Mover teeth length (mm)		210	
L_{stk}, Stack length (mm)		50	
F_f, Filling factor		0.45	
k_{sp}, Split ratio	0.75	0.70	0.70
k_{dc}, DC to total loss ratio	0.48	-	0.68
k_w, Winding factor	0.866	-	1
P_{loss}, copper loss (W)		180	
N_{ac}, Number of AC turns per slot	55	110	110
N_{dc}, Number of DC turns per slot	55	-	-
i_{ac}, AC component amplitude (A)	11.71	8.42	5.50
i_{dc}, DC component current (A)	8.20	-	5.65
Back EMF coefficient (V/(m/s))	2.9	-	12.1
Efficiency (%) @10m/s	65.23	74.9	78.3
f_t, Rated thrust force (N)	38.5	107.3	**104.5**
R_{rip}, Force ripple ratio (%)	8.1	85.3	**18.9**
D_t, Thrust force density(kN/m^3)	44.7	124.7	121.4
f_{max}, Peak thrust force (N)	111.2	194.2	180.9

Design parameters and performance metrics for the three machines are detailed in TABLE VIII and Fig. 19. TABLE VIII highlights that the VF-RLM displays the smoothest output thrust force. The output force is 38.5N on average. Due to the end effect, the 1st and 2nd order harmonics take up most of the force ripple, which is about 3.2N as shown in Fig. 19. The average force of SRLM is approximately 107.3N, as illustrated in Fig. 19. Due to the longitude end effect and commutation issue, the output thrust force of the machine mainly composed of the 2nd and 3rd order harmonics. Thanks to the boost effect of magnetic gear and slot space utilization improvement, the proposed VRLMs could achieve higher force compared to conventional VF-RLM. In contrast with the SRLM [26], thanks to the sinusoidal driving method, the proposed machine achieves a much lower thrust ripple with basically the same average force. Regarding overload capability, the maximum output thrust forces under conditions of three times the rated copper loss is 180.9N for the proposed machine, 194.2N for the SRLM, and 111.2N for the VF-RLM, respectively, which is summarized in Table VIII.

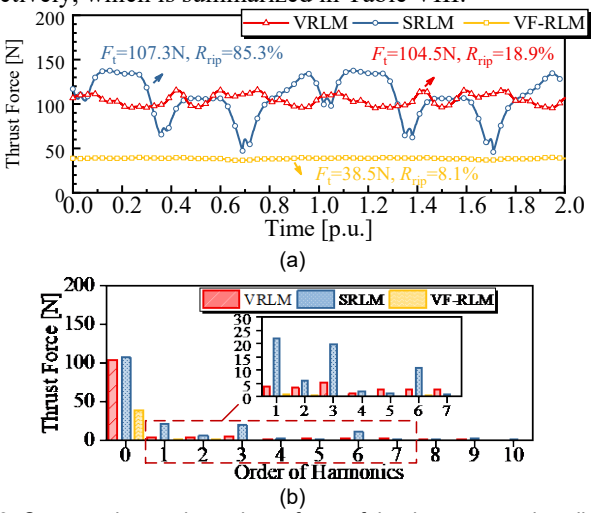

Fig. 19. Comparative study on thrust force of the three magnetless linear machine. (a) VF-RLM [7] (b) SRLM [26].

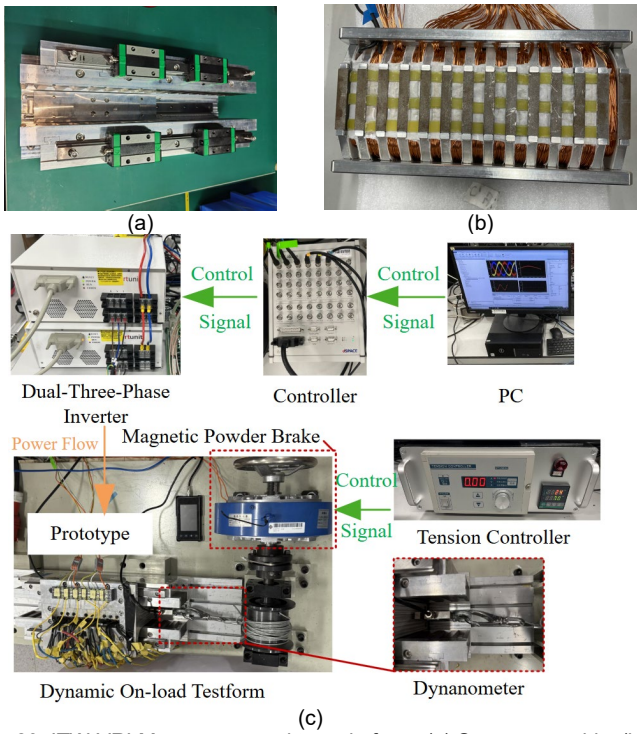

Fig. 20. ITW-VRLM prototype and test platform. (a) Stator assembly. (b) Mover assembly. (c) Prototype and test platform.

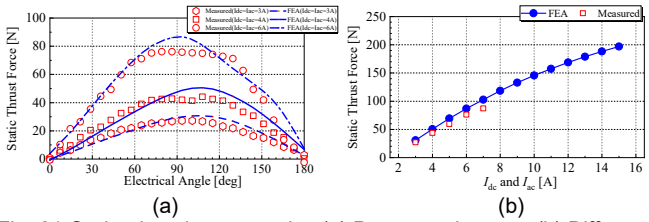

Fig. 21 On-load static test results. (a) Power angle curve (b) Different current density.

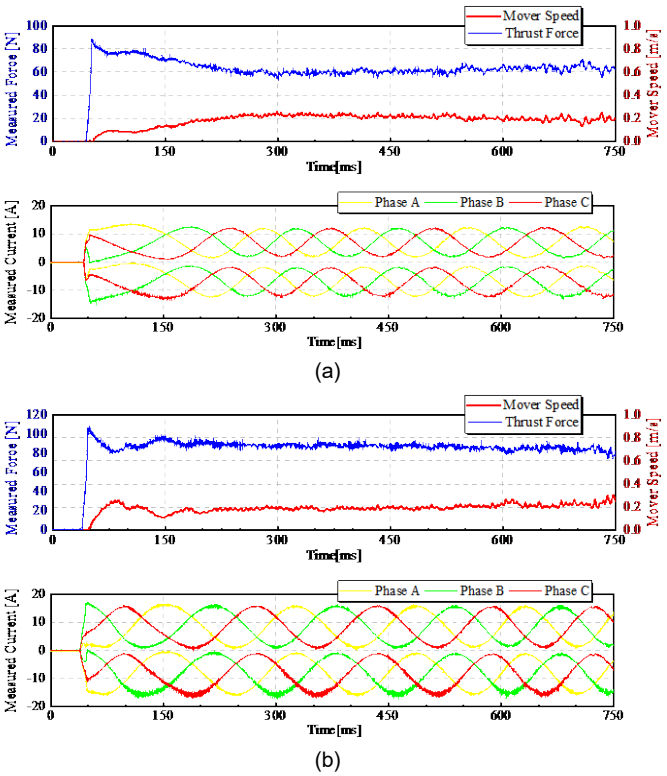

Fig. 22 On-load dynamic test results. *(a) Light-loaded. (b) Rated-loaded.*

V. Experimental Verification

The proposed topology and winding configuration's feasibility is verified through the manufacturing of a prototype based on the geometric parameters of the 12/7 machine listed in Table VII. The stator and mover incorporate DW300-35 laminated iron cores, with AWG 23 copper wire employing a parallel twisting of four strands. Fig. 20 details the prototype and its test platform, showcasing the rail stator assembly in Figure 20(a), the mover assembly in Fig. 20(b), and the test platform setup in Fig. 20(c), comprising a Magnetic powder brake, dynamometer, dSPACE controller, inverter, among other components, where dynamometric device is used to record the force waveform, the magnetic power brake is used to add the load to the prototype. The prototype and magnetic power brake are connected via rope.

Fig. 21(a) displays the static on-load test outcomes of the machine at various power angles ranging from 0 to 180 degrees, with I_{dc} and AC current amplitude I_{ac} values set at 3A, 4A, and 6A, representing light, medium, and heavy loads. Discrepancies between finite element analysis (FEA) and experimental results primarily stem from dynamometer limitations when applying pull and push forces consecutively within short timeframes, with errors escalating as loads increase. In Fig. 21(b), a comparison between FEA and experimental thrust forces across different current levels (1A to 15A) is presented. The experiment registers a maximum current of 7A, yielding an average thrust force of 87.1N, whereas the FEA simulation reaches 15A with a thrust force of 196.9N. The experimental results show good agreement with calculated results.

The dynamic assessment of the machine involves closed-loop speed control. Fig. 22 illustrates the dynamic trial of the prototype utilizing the Field-Oriented Control (FOC) algorithm, with the mover's target speed set at 0.2m/s. In Fig. 22(a), with I_{dc} set at 6A, the mover maintains a constant speed of 0.2 m/s under a 60N load force. At rated load force, Fig. 22(b) demonstrates the mover achieving 0.2 m/s speed under a 90N load force with I_{dc} set to 7.5A.

VI. Conclusion

In this paper, a novel integrated toroidal winding configuration is proposed for double-sided Vernier reluctance linear machine not only solve the space conflict between field and armature winding but simplify manufacturing process as well. By optimizing arrangements of excitations, the thrust density of the machine with ITW winding could reach 121.4kN/m^3, when using 12/7 slot/pole combination on the balance of average thrust force and force fluctuations. Thanks to the enhanced magnetic gear effect and sinusoidal driving method, the proposed winding configuration could obtain higher thrust force compared to conventional VF-RLM and lower thrust ripple in contrast with the SRLM.

This design, taking advantages of low cost and enhanced load capability, has great potential in industrial assembly line scenarios and other long stroke applications.

References

[1] I. Boldea, L. N. Tutelea, W. Xu, and M. Pucci, "Linear Electric Machines, Drives, and MAGLEVs: An Overview," IEEE Transactions on Industrial Electronics, vol. 65, no. 9, pp. 7504-7515, 2018, doi: 10.1109/tie.2017.2733492.

[2] Z. Li and S. Niu, "Overview on Variable Flux Reluctance Linear Machines for Long- Stroke Applications," IEEE Transactions on Transportation Electrification, pp. 1-1, 2024, doi: 10.1109/tte.2024.3389713.

[3] Z. Zhang, M. Luo, J.-a. Duan, and B. Kou, "Design and Modeling of a Novel Permanent Magnet Width Modulation Secondary for Permanent Magnet Linear Synchronous Motor," IEEE Transactions on Industrial Electronics, vol. 69, no. 3, pp. 2749-2758, 2022, doi: 10.1109/tie.2021.3065625.

[4] Q. Lu, Y. Li, Y. Ye, and Z. Q. Zhu, "Investigation of Forces in Linear Induction Motor Under Different Slip Frequency for Low-Speed Maglev Application," IEEE Transactions on Energy Conversion, vol. 28, no. 1, pp. 145-153, 2013, doi: 10.1109/tec.2012.2227114.

[5] J. Pan, Y. Zou, and G. Cao, "An asymmetric linear switched reluctance motor," IEEE Transactions on Energy conversion, vol. 28, no. 2, pp. 444-451, 2013.

[6] Y. Yang, X. Sun, N. Xu, B. Wan and M. Yao, "Design Optimization of a 12/10 Switched Reluctance Motor Considering Target Driving Cycle and Driving Condition," in IEEE Journal of Emerging and Selected Topics in Power Electronics, doi: 10.1109/JESTPE.2025.3545024.

[7] X. Sun, Y. Wen, Y. Zhu, L. Zhang, M. Yao and G. Lei, "FCS-MPC With Improved Prediction for Suppressing Torque and Current Pulsations of Switched Reluctance Motors," in IEEE Transactions on Industrial Electronics, doi: 10.1109/TIE.2024.3515281.

[8] M. Chowdhury, A. Tesfamicael, M. Islam, and I. Husain, "Design Optimization of a Synchronous Reluctance Machine for High-Performance Applications," IEEE Transactions on Industry Applications, vol. 57, no. 5, pp. 4720-4732, 2021, doi: 10.1109/tia.2021.3091416.

[9] J. Ou, Y. Liu, M. Schiefer, and M. Doppelbauer, "A Novel PM-Free High-Speed Linear Machine With Amorphous Primary Core," IEEE Transactions on Magnetics, vol. 53, no. 11, pp. 1-8, 2017, doi: 10.1109/tmag.2017.2701152.

[10] R. Cao, Y. Jin, Y. Zhang, and M. Cheng, "A New Double-Sided HTS Flux-Switching Linear Motor With Series Magnet Circuit," IEEE Transactions on Applied Superconductivity, vol. 26, no. 7, pp. 1-5, 2016, doi: 10.1109/tasc.2016.2593043.

[11] Z. Li, S. Niu, X. Zhao, and W. N. Fu, "Quantitive Harmonic Analysis and Force Ripple Suppression of a Parallel Complementary Modular Linear Reluctance Machine," IEEE Transactions on Energy Conversion, vol. 38, no. 2, pp. 789-799, 2023, doi: 10.1109/tec.2022.3221479.

[12] Y. Shen and Q. Lu, "Investigation of Novel Multi-Tooth Linear Variable Flux Reluctance Machines," IEEE Transactions on Magnetics, vol. 54, no. 11, pp. 1-5, 2018, doi: 10.1109/tmag.2018.2839662.

[13] Z. Zeng and Q. Lu, "Investigation of Novel Partitioned-Primary Hybrid-Excited Flux-Switching Linear Machines," IEEE Transactions on Industrial Electronics, vol. 65, no. 12, pp. 9804-9813, 2018, doi: 10.1109/tie.2017.2786205.

[14] Z. Li, X. Zhao, and S. Niu, "Novel High-Order-Harmonic Toroidal Winding Design Approach for Double-Sided Vernier Reluctance Linear Machine," IEEE Transactions on Industrial Electronics, vol. 70, no. 10, pp. 9823-9834, 2023, doi: 10.1109/tie.2022.3224133.

[15] S. Jia, P. Sun, D. Liang, X. Dong, Z. Zhu, and J. Liu, "Analysis of DC-Biased Vernier Reluctance Machines Having Distributed Windings," IEEE Transactions on Magnetics, vol. 57, no. 7, pp. 1-5, 2021, doi: 10.1109/tmag.2021.3074935.

[16] Y. Gao, R. Qu, D. Li, and F. Chen, "Force Ripple Minimization of a Linear Vernier Permanent Magnet Machine for Direct-Drive Servo Applications," IEEE Transactions on Magnetics, vol. 53, no. 6, pp. 1-5, 2017, doi: 10.1109/tmag.2017.2656178.
[17] Z. Q. Zhu and Y. Liu, "Analysis of Air-Gap Field Modulation and Magnetic Gearing Effect in Fractional-Slot Concentrated-Winding Permanent-Magnet Synchronous Machines," IEEE Transactions on Industrial Electronics, vol. 65, no. 5, pp. 3688-3698, 2018, doi: 10.1109/tie.2017.2758747.
[18] W. N. Fu, Y. Chen, and X. Guo, "Novel Dual-Layer and Triple-Layer Permanent-Magnet-Excited Synchronous Motors," IEEE Transactions on Magnetics, vol. 51, no. 11, pp. 1-4, 2015, doi: 10.1109/tmag.2015.2435795.
[19] R. Cao, M. Cheng, C. C. Mi, and W. Hua, "Influence of Leading Design Parameters on the Force Performance of a Complementary and Modular Linear Flux-Switching Permanent-Magnet Motor," IEEE Transactions on Industrial Electronics, vol. 61, no. 5, pp. 2165-2175, 2014, doi: 10.1109/tie.2013.2271603.
[20] S. Niu, T. Sheng, X. Zhao, and X. Zhang, "Operation Principle and Torque Component Quantification of Short-Pitched Flux-Bidirectional-Modulation Machine," IEEE Access, vol. 7, pp. 136676-136685, 2019, doi: 10.1109/access.2019.2942482.
[21] S. Jia, R. Qu, J. Li, and D. Li, "Principles of Stator DC Winding Excited Vernier Reluctance Machines," IEEE Transactions on Energy Conversion, vol. 31, no. 3, pp. 935-946, 2016, doi: 10.1109/tec.2016.2538773.
[22] X. Zhao, S. Wang, S. Niu, W. Fu, and X. Zhang, "A Novel High-Order-Harmonic Winding Design Method for Vernier Reluctance Machine With DC Coils Across Two Stator Teeth," IEEE Transactions on Industrial Electronics, vol. 69, no. 8, pp. 7696-7707, 2022, doi: 10.1109/tie.2021.3104589.
[23] Z. Yu, C. Gan, Y. Chen, and R. Qu, "DC-Biased Sinusoidal Current Excited Switched Reluctance Motor Drives Based on Flux Modulation Principle," IEEE Transactions on Power Electronics, vol. 35, no. 10, pp. 10614-10628, 2020, doi: 10.1109/tpel.2020.2975121.
[24] S. Jia, P. Chen, X. Dong, D. Liang, B. Li, and J. Liu, "Modeling and Current Control Strategy for Novel Two-Phase DC-Biased Vernier Reluctance Machine," IEEE Transactions on Industry Applications, vol. 59, no. 1, pp. 814-822, 2023, doi: 10.1109/tia.2022.3216557.
[25] X. Zhao, S. Niu and W. Fu, "Sensitivity Analysis and Design Optimization of a New Hybrid-Excited Dual-PM Generator with Relieving-DC-Saturation Structure for Stand-Alone Wind Power Generation," in IEEE Transactions on Magnetics, vol. 56, no. 1, pp. 1-5, Jan. 2020, Art no. 7504105, doi: 10.1109/TMAG.2019.2951078.
[26] J. Du, D. Liang and X. Liu, "Performance Analysis of a Mutually Coupled Linear Switched Reluctance Machine for Direct-Drive Wave Energy Conversions," in IEEE Transactions on Magnetics, vol. 53, no. 9, pp. 1-10, Sept. 2017, Art no. 8108110, doi: 10.1109/TMAG.2017.2721363.
[27] M. A. Kabir and I. Husain, "Design of Mutually Coupled Switched Reluctance Motors (MCSRMs) for Extended Speed Applications Using 3-Phase Standard Inverters," in IEEE Transactions on Energy Conversion, vol. 31, no. 2, pp. 436-445, June 2016, doi: 10.1109/TEC.2015.2499086.

Zhenghao Li received the B.Sc. degree in electrical engineering from South China University of Technology, Guangzhou, China, in 2016, the M.Sc. degree in electrical engineering from University of Chinese Academy of Sciences, Beijing, China, in 2019 and the Ph.D. degree from Hong Kong Polytechnic University, Hong Kong, in 2023. He is currently working as postdoctoral researcher in Hong Kong Polytechnic University. His research interests include Reluctance Linear Machines and Drives.

Shuangxia Niu received the B.Sc. and M.Sc. degrees in electrical engineering from Tianjin University, China, in 2002 and 2005, respectively, and the Ph.D. degree from The University of Hong Kong, Hong Kong, in 2009. She is currently working as Professor with the Department of Electrical and Electronic Engineering, The Hong Kong Polytechnic University, Hong Kong. Her research interests include the Electric Vehicle Technologies, Renewable Energy Systems, Machines and Drives, Power Electronics technology, Applied Electromagnetic, Numerical Method and Optimization.

Mingyuan Jiang received the B.Eng. degree in electrical engineering and automation from Shanghai Maritime University, Shanghai, China, in 2020, and the M.Sc. and Ph.D. degrees in electrical engineering from The Hong Kong Polytechnic University, Hong Kong, China, in 2021 and 2024. He is currently a Research Assistant Professor in the Department of Electrical and Electronic Engineering, The Hong Kong Polytechnic University. His primary research focuses on the design, optimization, and control of electric machines, electric vehicles, and power generation.

Zekai Lyu received the B.Eng. degree from Southwest Jiaotong University, Chengdu, China, in 2018, the M.Sc. degree from Harbin Institute of Technology, Harbin, China, in 2020, and the Ph.D. degree from Zhejiang University, Hangzhou, China, in 2024, all in electrical engineering.
He is currently a Postdoctoral Fellow with the Department of Electrical and Electronic Engineering, The Hong Kong Polytechnic University, Hong Kong SAR, China. His research interests include wide-bandgap device applications, electrical machines, and machine drives.

Wei Liu Wei Liu (Senior Member, IEEE) received the B.Eng. and M.Eng. degrees in electrical engineering from China University of Petroleum, Qingdao, China, in 2014 and 2017, respectively, and the Ph.D. degree in electrical and electronic engineering from The University of Hong Kong (HKU), Hong Kong, China, in 2021. He is currently an Assistant Professor with the Research Centre for Electric Vehicles and Department of Electrical and Electronic Engineering, The Hong Kong Polytechnic University (PolyU), Hong Kong, China. His research interests include wireless power transfer, power electronics, biomedical power electronics, and electric vehicle technologies.

K.T. Chau (Fellow, IEEE) received the B.Sc. (Eng.), M.Phil., and Ph.D. degrees in electrical and electronic engineering from The University of Hong Kong, Hong Kong, China, in 1988, 1991, and 1993, respectively. He serves as a Chair Professor in electrical energy engineering with the Research Centre for Electric Vehicles and Department of Electrical and Electronic Engineering, The Hong Kong Polytechnic University. His research interests include electric and hybrid vehicles, power electronics and drives, and renewable energies. He is the author of nine books and more than 350 journal papers. Prof. Chau is a Fellow of the Institution of Engineering and Technology (IET), U.K., and the Hong Kong Institution of Engineers. He is also a Co-Editor of the Journal of Asian Electric Vehicles. He is a Chartered Engineer. He was the recipient of the Changjiang Chair Professorship from the Ministry of Education, China, and the Environmental Excellence in Transportation Award for Education, Training, and Public Awareness from the Society of Automotive Engineers International.